Effects of boron addition on the high temperature oxidation of $MoSi_2$ alloys

Ding, Zhaoying; Brouwer, Johannes C.; Zhu, Jia Ning; Popovich, Vera; Hermans, Marcel J.M.; Sloof, Willem G.

DOI
10.1016/j.scriptamat.2023.115580

Publication date
2023

Document Version
Final published version

Published in
Scripta Materialia

Scripta Materialia 234 (2023) 115580

Contents lists available at ScienceDirect

Scripta Materialia

journal homepage: www.journals.elsevier.com/scripta-materialia

Effects of boron addition on the high temperature oxidation of $MoSi_2$ alloys

Zhaoying Ding, Johannes C. Brouwer, Jia-Ning Zhu, Vera Popovich, Marcel J.M. Hermans, Willem G. Sloof *

Department of Materials Science and Engineering, Delft University of Technology, Mekelweg 2, Delft, CD 2628, the Netherlands

ARTICLE INFO

Keywords:
Boron
Oxidation
$MoSi_2$
Kinetics

ABSTRACT

Boron containing $MoSi_2$ is a promising material for applications at high temperature, but the oxidation mechanism is still unclear. In this work, the high temperature (1100 °C) oxidation of B doped $MoSi_2$ in synthetic air has been investigated. A (boro)silicate layer is formed on the surface of the alloy, which features a mixture of amorphous SiO_2 and cristobalite. After an initial transient period, the oxidation kinetics follows a parabolic growth rate law. The growth rate constant of the oxide layer is enhanced by the boron in the alloy by 90 % per at. % B. The increase in growth rate is associated with boron mitigating the formation of cristobalite thereby promoting the formation of amorphous SiO_2.

With a high melting point of over 2000 °C, moderate density (6.24 g/cm^3) and outstanding oxidation resistance, molybdenum disilicide ($MoSi_2$) is one of the most promising high-temperature material used as furnace elements, high-temperature heat exchangers and filters, gas burners, components for hot-section jet engines and gas turbines [1,2]. However, it suffers from pest oxidation at temperatures of 400–600 °C [3] through the diffusion of oxygen along grain boundaries [4], resulting in rapid fragmentation and disintegration. It is suggested that having crystalline cristobalite as the oxide scale for $MoSi_2$ can also accelerate the pest oxidation. To resolve this problem, a minor amount of boron is added to $MoSi_2$, which also allows to enhance the fracture toughness of the alloy [1]. A borosilicate layer with a lower viscosity than silica is formed on the surface of Mo–Si–B alloy upon oxidation [4,5], which promotes a faster coverage and provides a self-healing effect on the surface of the alloy [6]. Also B-containing $MoSi_2$ particles are used for crack-healing in yttria partially stabilized zirconia (YPSZ) [7], where the presence of B significantly facilitates the formation of borosilicate as crack-filling agent and thereby promotes the subsequent formation of the mechanical load bearing phase of zircon [8].

Although the oxidation kinetics of $MoSi_2$ with and without boron addition has been studied [9–15], the effect of boron on the high temperature oxidation of $MoSi_2$ is still debated [3,9]. Moreover, electron beam induced damage caused by high diffuse electron scattering as in electron microscopy may result in transformation of crystalline into amorphous SiO_2 hindering detailed microstructure analysis [16,17]. To date, the evolution of the microstructure on an atomic scale to reveal the oxidation mechanism of $MoSi_2$ with boron addition is still lacking [18]. Thus, the present study aims at understanding the effect of boron addition on the oxidation of $MoSi_2$ at elevated temperature.

Pure $MoSi_2$ powder (<50 μm, ChemPUR GmbH, Germany) and $MoSi_2$ with boron addition powder (<45 μm, nominal 2 wt.% boron, ChemPUR GmbH, Germany) were used as the starting material. Also, a mixture of both powders, i.e., $MoSi_2$ without and with 2 wt.% B, with a ratio of 1:1 was prepared to obtain $MoSi_2$ with 1 wt.% B particles. The starting powders and their mixtures were milled using a planetary ball mill (PM100, Retsch GmbH, Germany) to refine the microstructure of molybdenum boride. The ball-milling of the powders was conducted in around 20 ml isopropanol using ZrO_2 balls (100 and 8 balls with diameter of 5 mm and 10 mm, respectively) and a 50 ml ZrO_2 jar. The weight ratio of balls and powder was about 20:1. In order to confirm the boron content of the material, the ball milled powders were analysed using inductively couple plasma optical emission spectroscopy (ICP-OES, iCAP 6500 Duo Thermo Fisher Scientific). The dissolution of these powders was specifically designed for the Mo–Si–B system [19]. The measured content of boron in the ball milled powders are 0 wt.%, 0.66 wt.% (3 at.%) and 1.29 wt.% (6 at.%), respectively; see Table S1 in Supplementary Material.

Next, the above ball milled powders were densified by means of spark plasma sintering (SPS) using a HP D 25 SD furnace (FCT Systeme GmbH, Germany) with a sintering pressure of 50 MPa at 1500 °C for 30 min in a flowing argon atmosphere. The heating rate was 20 °C/min, while natural cooling was used to cool down from the maximum

* Corresponding author.
E-mail address: w.g.sloof@tudelft.nl (W.G. Sloof).

https://doi.org/10.1016/j.scriptamat.2023.115580
Received 21 February 2023; Received in revised form 18 April 2023; Accepted 24 May 2023
Available online 27 May 2023

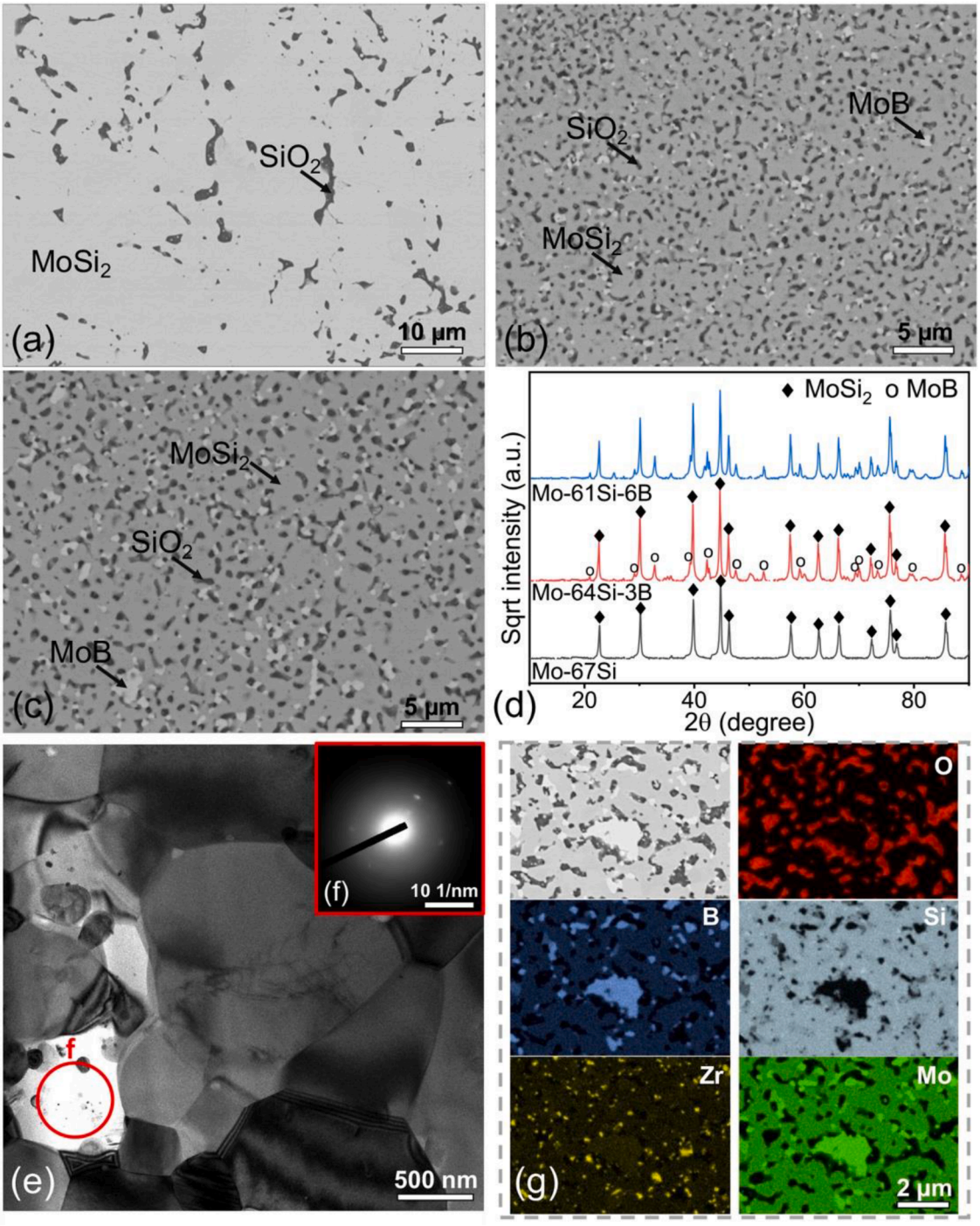

Fig. 1. SEM back scattered electron images of the microstructure of Mo–Si–B alloys: (a) Mo–67Si, (b) Mo–64Si–3B and (c) Mo–61Si–6B; (d) X-ray diffraction patterns of the Mo–Si–B alloys; (e) bright-field TEM image of Mo–61Si–6B; (f) SAED pattern of the area in (e) showing amorphous SiO_2; (g) X-ray emission maps of the elements in Mo–61Si–6B

temperature. The prepared alloys with 0, 3 and 6 at.% boron are denoted as Mo–67Si, Mo–64Si–3B and Mo–61Si–6B, respectively.

The Mo–67Si alloy features a microstructure with a matrix of $MoSi_2$ and small SiO_2 inclusions, see Fig. 1a, while Mo–64Si–3B and Mo–61Si–6B feature a microstructure also with a matrix of $MoSi_2$ and homogeneous distributed MoB precipitates but with more SiO_2 inclusions; see Fig. 1b and c. The diffractograms of the densified materials with different amount of boron addition clearly show peaks of tetragonal $MoSi_2$ as the main phase and small peaks of tetragonal MoB as the minor second phase; see Fig. 1d. The inclusions of SiO_2 are not seen in the diffractogram due to their amorphous nature; see Fig. 1e and f. The elemental mapping, shown in Fig. 1g, confirms the indicated phases and the contamination of Zr from the ball milling.

The isothermal oxidation kinetics of the Mo–Si–B material in dry synthetic air (N_2 with 20 vol.% O_2) at a temperature of 1100 °C in terms of mass change was assessed via thermogravimetric analyses, using a dual furnace balance (Setaram TAG 16/18, France). To this end, the sintered discs were cut into rectangular bars of 15 × 8 × 2 mm via electric discharge machining (EDM). The initial mass of the sample was weighed using a Mettler Toledo balance (accuracy ± 1 μg). A dummy

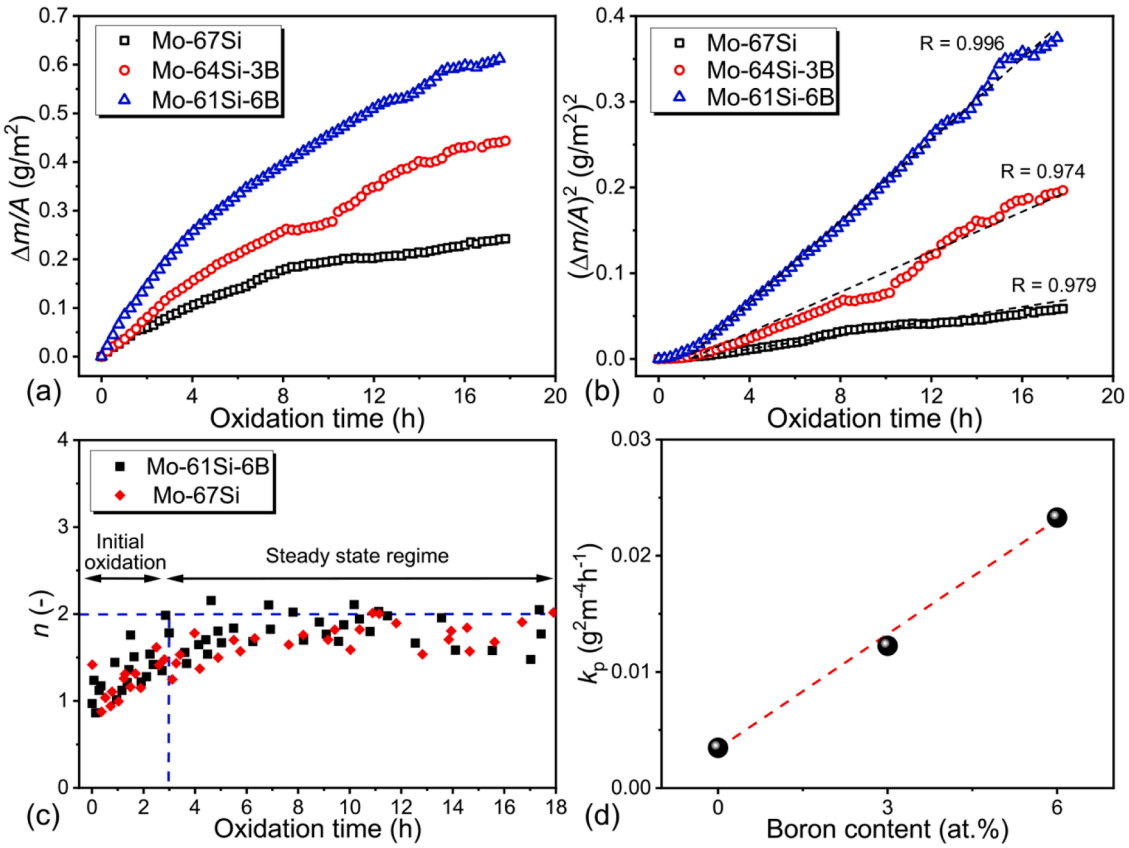

Fig. 2. Thermogravimetric analysis of the oxidation of Mo–Si–B at 1100 °C in synthetic air as a function of oxidation time in terms of (a) weight gain per unit area; (b) squared weight gain per unit area; (c) exponent n of a power law (cf. Eq. 1); and (d) parabolic oxide growth rate constant k_p as a function of the alloy boron content (red dashed line only to guide the eyes).

sample of alumina with the same dimensions was mounted onto a sapphire rod of the counter part of the balance to eliminate any buoyancy effect. The gas mixture was admitted to the TGA analyser via mass flow controllers (Bronkhorst, the Netherlands) such that the total gas flow matches 50 sccm, which was equally divided over both furnace tubes, i.e., 25 sccm gas in each furnace. To flush the gas lines, balance and furnaces, the TGA system was pumped to vacuum (< 50 Pa) and refilled with Ar three times. Then, the dual furnaces were heated up from room temperature to the target temperature with 10 °C/min. When the target temperature for isothermal oxidation was reached, the gas composition was switched to the oxidation atmosphere while maintaining a total gas flow of 50 sccm for 20 h. After oxidation, the furnace was cooled down to room temperature with 10 °C/min while flushing with pure Ar. Details of the oxide scale composition and microstructure analyses methods can be found in the Supplementary Material.

The weight gain per unit surface area of the Mo–Si–B alloys recorded during oxidation at 1100 °C in synthetic air is shown in Fig. 2a. Although the weight gain during this oxidation process is very small, it can be observed clearly that the weight gain increases with increasing boron content of the Mo–Si–(B) alloys. The linear fits of the mass gain versus oxidation time in Fig. 2b suggest that the oxide layer growth obeys a parabolic growth rate law after an initial transient oxidation period. This

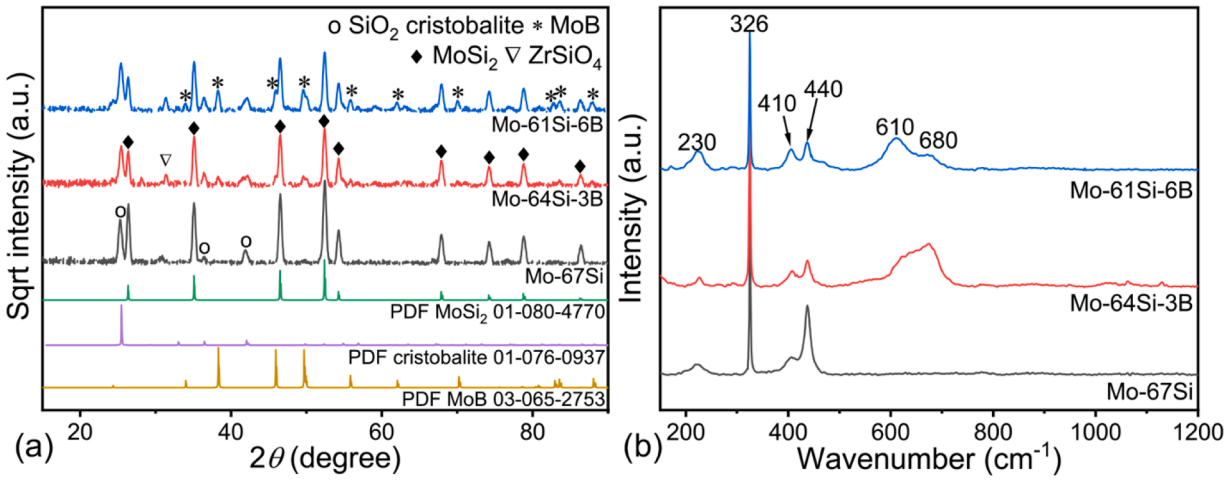

Fig. 3. (a) XRD patterns recorded with grazing incidence geometry and (b) Raman spectra of Mo–Si–B alloys after oxidation at 1100 °C in synthetic air for 20 h.

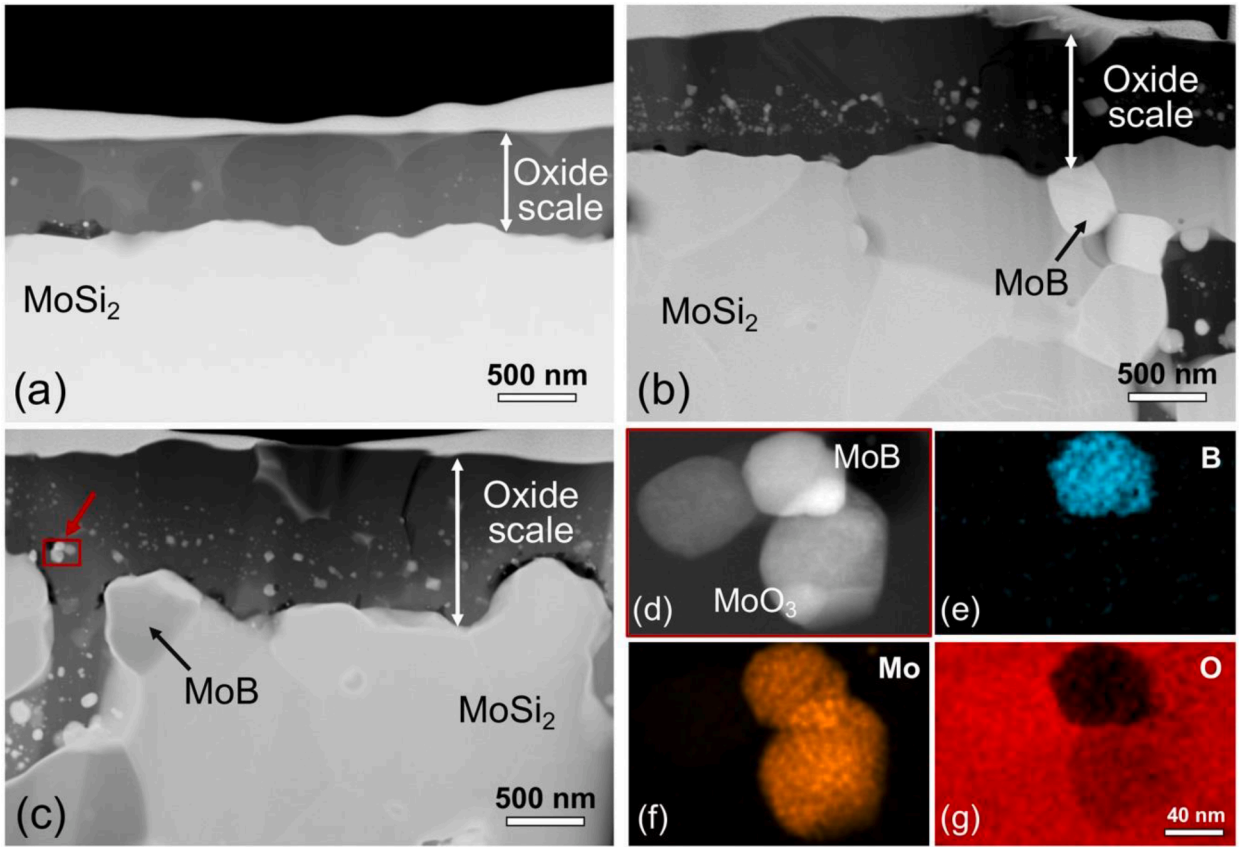

Fig. 4. STEM image (HAADF) of cross-section of Mo–Si–B alloys after oxidation at 1100 °C in synthetic air for 20 h: (a) Mo–67Si, (b) Mo–64Si–3B and (c) Mo–61Si–6B; and (d) image of area indicated by the red box in (c) with (e), (f) and (g) the corresponding X-ray emission maps of B, Mo and O, respectively.

indicates that the oxidation is dominated by diffusion during the steady state regime. The growth of the silica or borosilicate layer occurs by diffusion of oxygen through the developing layer. It has been reported that two main mechanisms are possible: O_2 permeation through the structure and O^{2-} self-diffusion through the network of bonded oxygen via point defects, respectively [20]. Thus, the rate-limiting step in the oxidation of $MoSi_2$ is the inward diffusion of O^{2-} or O_2 through the developing continuous SiO_2 layer [8,18].

In an attempt to describe the oxidation process quantitatively, the oxidation kinetics was formulated as a power law with exponent n [21]:

$$\left(\frac{\Delta m}{A}\right)^n = k_m t \tag{1}$$

where Δm is the weight change; A is the surface area of the sample and t the isothermal oxidation time; k_m denotes the oxidation rate constant. The exponent n versus time t can be derived from the mass change data with [22]:

$$\frac{1}{n} = \frac{\partial \log\left(\frac{\Delta m}{A}\right)}{\partial \log(t)} \tag{2}$$

Analysis of the exponent n as a function of oxidation time of the oxide growth curves shows that the oxide growth proceeds a transition from an initial linear growth rate to a parabolic growth rate regime; see Fig. 2c. A slightly shortened transient stage in the Mo–61Si–6B than Mo–67Si alloy can be seen in Fig. 2c, indicating a faster complete coverage of boron doped SiO_2 (borosilicate). The parabolic growth rate constant increases proportional with the boron content of Mo–Si–(B) alloy; see Fig. 2d. In practice, the enhanced rate is still acceptable, since it promotes the complete coverage of the $MoSi_2$ alloy by a protective oxide scale which is the key to oxidation resistance.

After oxidation of the alloys in dry synthetic air at 1100 °C for 20 h, their surfaces are covered with an oxide scale of SiO_2; see Fig. S1 in Supplementary Material. It can be observed that the boron promotes the formation of a smooth and glassy film on Mo–Si–B. Cristobalite with a tetragonal crystal lattice in the silica layer formed on Mo–Si–(B) alloys was identified with XRD using a grazing incidence geometry; see Fig. 3a. In addition, the peaks at 230 and 410 cm^{-1} in the Raman spectra (Fig. 3b) of the oxidized Mo–Si–(B) alloys can be assigned to the A_1 modes from cristobalite [23,24]. Further, two Raman active lattice modes are clearly seen in Fig. 3b, namely an A_{1g} mode and an E_g mode at 326 and 440 cm^{-1}, respectively, both pertaining to t-$MoSi_2$ [25]. A significant band in the 610–680 cm^{-1} region can be observed in the Raman spectra of the oxidized Mo–64Si–3B and Mo–61Si–6B alloys, but not in the spectrum of oxidized pure $MoSi_2$; see Fig. 3b. The band in the 610–630 cm^{-1} region is associated to vibrations of metaborate anions of the ring type [26]. The band near 680 cm^{-1} is associated with the bending motion of oxygen bonds contributing to defect structures [26]. These defect structures have been reported to consist of broken oxygen bridges within the silicate network, which hints at an amorphous structure of the oxide formed on the alloys with boron.

Cross-sections of the oxidized alloys confirm a continuous and dense SiO_2 film of which the thickness increases with alloy B content; see Fig. 4a–c. In the oxide layer grown on the Mo–64Si–3B and Mo–61Si–6B alloys, inclusions with a size of about 40 nm can be seen near the interface with the alloy; see Fig 4b and c. Local composition analysis with X-ray micro analysis (XMA) indicates that these inclusions are a mix of MoB and MoO_3; see Fig. 4d–g.

High-resolution transmission electron microscopy (HRTEM) of the oxide scale formed on Mo–67Si alloy show crystalline fragments in the SiO_2 scale; see Fig. 5a. The D-spacing of these crystalline fragments are 0.49 and 0.28 nm, respectively, which can be assigned to (100) and (012) lattice planes of cristobalite having a tetragonal structure; see

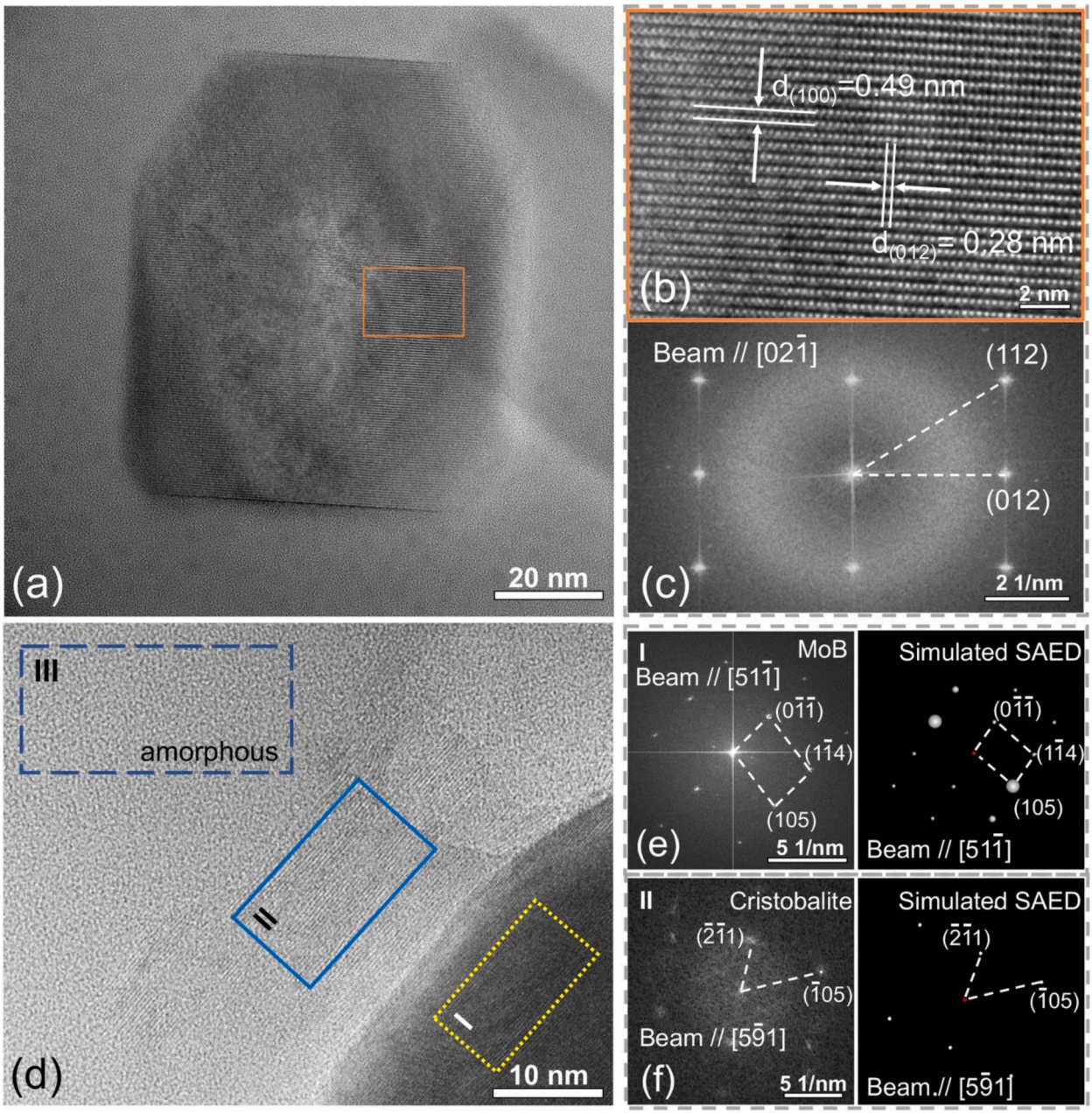

Fig. 5. Evidence of cristobalite nanocrystals from HRTEM after oxidation at 1100 °C in synthetic air for 20 h: (a)–(c) belongs to Mo–67Si and (d)–(f) belongs to Mo–61Si–6B; (a) HRTEM image of the oxide scale grown on Mo–67Si showing crystalline SiO_2 patch in the amorphous SiO_2; (b) HRTEM image of the frame area in (a); (c) FFT of image (b); (d) HRTEM image of MoB-SiO_2 edge in the oxide scale on Mo–61Si–6B; (e) FFT of region I in HRTEM image (d) and simulated SAED by PDF-4+ software (version 2023) showing the orientation of MoB atomic layers; (f) FFT of region II in HRTEM image (d) and simulated SAED of cristobalite SiO_2. Region III in HRTEM image (d) shows amorphous SiO_2.

Fig. 5b. The diffraction pattern obtained by Fast Fourier transformation (FFT) of the HRTEM image confirms that the crystalline phase is tetragonal cristobalite; see Fig. 5c. SiO_2 with an amorphous structure surrounding the cristobalite fragments was also observed in the silica scale on pure $MoSi_2$ (see Fig. 5a), which is likely ascribed to high diffuse electron scattering intensities (DSIs) [16,17].

Such crystalline SiO_2 fragments can hardly be found in the oxide scale formed on Mo–64Si–3B and Mo–61Si–6B. Only near the interface with MoB small orderly arranged atoms clusters were observed within the amorphous oxide scale of SiO_2; see Fig. 5d. FFT of these regions in the HRTEM image shows that the pattern matches well with the simulated diffraction pattern of tetragonal cristobalite. Thus, the presence of B promotes the formation of amorphous structure in the SiO_2 scale. As a reference, the FFT of the lattice fringes in the HRTEM image pertaining to the MoB phase was also performed and the pattern matches well with the simulated SAED pattern of tetragonal MoB. The amount of cristobalite in the SiO_2 layer reduces with increasing boron content in the Mo–Si–B alloy which also indicates that boron effectively promotes the formation of amorphous SiO_2.

Upon oxidation, the MoB in the alloy is oxidized resulting in B_2O_3, which dissolves in SiO_2 as a network modifier [27]. Then, some Si–O bonds are broken, which is beneficial for vitrification and hinders crystallization of SiO_2 [28]. This change of the local order of SiO_2 enhances the diffusivity of oxygen. Since the diffusion channels in cristobalite are smaller in size than the mean of those in amorphous SiO_2, the O_2 permeation is heavily suppressed in a crystalline SiO_2 when

compared to the enlarged ring channels in SiO_2 glass [29,30]. It has been reported that the diffusivity of oxygen in amorphous SiO_2 is about five times greater than that in cristobalite at high temperature [20], which explains the enhanced diffusion-controlled oxidation of Mo–Si–(B) alloys with increasing boron addition.

In conclusion, the high temperature oxidation in air of Mo–Si alloys is accelerated by addition of boron. The parabolic growth rate constant of the silica oxide layer increases proportional with the alloy boron content by 90 % per at.% B; with respect to the alloy without boron. The addition of boron effectively mitigates the formation of cristobalite and promotes the formation of amorphous SiO_2, which provides enlarged channels for oxygen diffusivity. The enhanced rate caused by boron addition is acceptable since it promotes the formation of a smooth protective oxide scale and prevents other accelerated degradation like pesting.

Declaration of Competing Interest

The authors declare that they have no known competing financial interests or personal relationships that could have appeared to influence the work reported in this paper.

Acknowledgment

This project has received funding from European Union Seventh Framework Programme (FP7/2007–2013) under grant agreement No. 309849, SAMBA. China Scholarship Council is acknowledged by Zhaoying Ding for their support (Grant No. 201806120145). The authors thank Dr. Frans D. Tichelaar for TEM analysis, Ing. R.W.A. Hendrikx for the XRD analysis and Ing. M.M. van den Brink for the ICP-OES analysis.

Supplementary materials

Supplementary material associated with this article can be found, in the online version, at doi:10.1016/j.scriptamat.2023.115580.

References

[1] J.A. Lemberg, R.O. Ritchie, Mo-Si-B alloys for ultrahigh-temperature structural applications, Adv. Mater. 24 (26) (2012) 3445–3480.
[2] J. Petrovic, $MoSi_2$-based high-temperature structural silicides, MRS Bull. 18 (1993) 35–41.
[3] S.H. Wen, J.B. Sha, Isothermal and cyclic oxidation behaviours of $MoSi_2$ with additions of B at 1250 °C prepared by spark plasma sintering, Mater. Charact. 139 (2018) 134–143.
[4] S.H. Wen, C.G. Zhou, J.B. Sha, Improvement of oxidation resistance of a Mo-62Si-5B (at.%) alloy at 1250 °C and 1350 °C via an *in situ* pre-formed SiO_2 fabricated by spark plasma sintering, Corros. Sci. 127 (2017) 175–185.
[5] J.S. Park, R. Sakidja, J.H. Perepezko, Coating designs for oxidation control of Mo–Si–B alloys, Scr. Mater. 46 (2002) 765–770.
[6] F.A. Rioult, S.D. Imhoff, R. Sakidja, J.H. Perepezko, Transient oxidation of Mo–Si–B alloys: effect of the microstructure size scale, Acta Mater. 57 (15) (2009) 4600–4613.
[7] Z. Derelioglu, A.L. Carabat, G.M. Song, S.V.D. Zwaag, W.G. Sloof, On the use of B-alloyed $MoSi_2$ particles as crack healing agents in yttria stabilized zirconia thermal barrier coatings, J. Eur. Ceram. Soc. 35 (16) (2015) 4507–4511.
[8] F. Nozahic, A.L. Carabat, W. Mao, D. Monceau, C. Estournes, C. Kwakernaak, S. van der Zwaag, W.G. Sloof, Kinetics of zircon formation in yttria partially stabilized zirconia as a result of oxidation of embedded molybdenum disilicide, Acta Mater. 174 (2019) 206–216.
[9] Z. Chen, W. Shao, M. Li, Z. Wu, P. Peng, C. Zhou, Effect of minor B modification on the oxidation behavior of $MoSi_2$ alloy at high temperature, Corros. Sci. 216 (2023).
[10] X.Q. Liu, Z.M. Guo, C. Ma, T. Lin, Microstructure of $MoSi_2$ coating with B addition prepared by vacuum cladding, Adv. Mater. Res. 468-471 (2012) 2111–2114.
[11] J. Pang, W. Wang, C. Zhou, Microstructure evolution and oxidation behavior of B modified $MoSi_2$ coating on Nb–Si based alloys, Corros. Sci. 105 (2016) 1–7.
[12] A.Y. Potanin, Y.S. Pogozhev, E.A. Levashov, A.V. Novikov, N.V. Shvindina, T. A. Sviridova, Kinetics and oxidation mechanism of $MoSi_2$–MoB ceramics in the 600–1200 °C temperature range, Ceram. Int. 43 (13) (2017) 10478–10486.
[13] P.R. Taleghani, S.R. Bakhshi, M. Erfanmanesh, G.H. Borhani, R. Vafaei, Improvement of $MoSi_2$ oxidation resistance via boron addition: fabrication of MoB/$MoSi_2$ composite by mechanical alloying and subsequent reactive sintering, Powder Technol. 254 (2014) 241–247.
[14] C.D. Wirkus, D.R. Wilder, High-temperature oxidation of molybdenum disilicide, J. Am. Ceram. 49 (4) (1966) 173–177.
[15] D.A. Berztiss, R.R. Cerchiara, E.A. Gulbransen, F.S. Pettit, G.H. Meier, Oxidation of $MoSi_2$ and comparison with other silicide materials, Mater. Sci. Eng. A 155 (1992) 165–181.
[16] A. Cernok, K. Marquardt, R. Caracas, E. Bykova, G. Habler, H.P. Liermann, M. Hanfland, M. Mezouar, E. Bobocioiu, L. Dubrovinsky, Compressional pathways of alpha-cristobalite, structure of cristobalite X-I, and towards the understanding of seifertite formation, Nat. Commun. 8 (2017) 15647.
[17] C.H. Chao, H.Y. Lu, β-Cristobalite stabilization in (Na_2O + Al_2O_3)-added silica, Metall. Mater. Trans. A 33A (2002) 2703–2711.
[18] S. Knittel, S. Mathieu, M. Vilasi, The oxidation behaviour of uniaxial hot pressed $MoSi_2$ in air from 400 to 1400 °C, Intermetallics 19 (8) (2011) 1207–1215.
[19] Y. Danzaki, K. Wagatsuma, T. Syoji, K. Yoshimi, Dissolution of molybdenum-silicon (-boron) alloys using a mixture of sulfuric, nitric and hydrofluoric acids and a sequential correction method for ICP-AES analysis, Fresenius J. Anal. Chem. 369 (2001) 184–186.
[20] J. Rodríguez-Viejo, F. Sibieude, M.T. Clavaguera-Mora, C. Monty, ^{18}O diffusion through amorphous SiO_2 and cristobalite, Appl. Phys. Lett. 63 (14) (1993) 1906–1908.
[21] D.J. Young, High Temperature Oxidation and Corrosion of Metals, Elsevier, 2008.
[22] Z. Ding, J.C. Brouwer, C. Kwakernaak, M.J.M. Hermans, V. Popovich, W. J. Quadakkers, W.G. Sloof, Selective oxidation of aluminium in $Mo(Al,Si)_2$, Corros. Sci. (2023) 211.
[23] J. Etchepare, M. Merian, P. Kaplan, Vibrational normal modes of SiO_2. II. cristobalite and tridymite, J. Chem. Phys. 68 (4) (1978) 1531–1537.
[24] J.B. Bates, Raman spectra of α and β cristobalite, J. Chem. Phys. 57 (1972) 4042–4047.
[25] G.A. Yakaboylu, T. Yumak, K. Sabolsky, E.M. Sabolsky, Effect of high temperature preoxidation treatment on the oxidation behavior of $MoSi_2$- and WSi_2–Al_2O_3 composites, J. Alloys Compd. 816 (2020), 152499.
[26] J. Kline, M. Tangstad, G. Tranell, A raman spectroscopic study of the structural modifications associated with the addition of calcium oxide and boron oxide to silica, Metall. Mater. Trans. B 46 (1) (2014) 62–73.
[27] B. Liang, Z.H. Yang, D.C. Jia, J.C. Rao, D.L. Yu, Y.J. Tian, Q. Li, Y. Miao, Q.S. Zhu, Y. Zhou, Amorphous silicoboron carbonitride monoliths resistant to flowing air up to 1800 °C, Corros. Sci. 109 (2016) 162–173.
[28] M.I. Ojovan, W.E. Lee, M.I. Ojovan, W.E. Lee, 17-Immobilisation of radioactive waste in glass. An Introduction to Nuclear Waste Immobilisation, 2nd Ed., Elsevier, Oxford, 2014, pp. 245–282.
[29] M.I. Heggie, R. Jones, C.D. Latham, S.C.P. Maynard, P. Tole, Molecular diffusion of oxygen and water in crystalline and amorphous silica, Philos. Mag. B 65 (3) (2006) 463–471.
[30] M.A. Lamkin, F.L. Riley, Oxygen mobility in silicon dioxide and silicate glasses: a review, J. Eur. Ceram. Soc. 10 (1992) 347–367.